A numerical study on the permeability in a tensorial form for laminar flow in anisotropic porous media

S. A. Galindo-Torres,[1,2,*] A. Scheuermann,[1] and L. Li[2]

[1] *Geotechnical Engineering Centre. School of Civil Engineering, The University of Queensland, Brisbane QLD 4072, Australia*

[2] *National Centre for Groundwater Research & Training. School of Civil Engineering, The University of Queensland, Brisbane QLD 4072, Australia*

Pore-scale flow simulations were conducted to investigate the permeability tensor of anisotropic porous media constructed using the Voronoi tessellation method. This construction method enabled the introduction of anisotropy to the media at the particle level in a random and yet controllable way. Simulations were carried out for media with different degrees of anisotropy through varying the mean aspect ratio of grain particles. The simulation results were then analysed using the Kozeny-Carman (KC) model. The KC model describes the permeability of the anisotropic media in a tensor form with the anisotropy represented by different tortuosities along the three principal directions. The tortuosity tensor was found to be a complex function of the particle morphology, which is yet to be fully determined. However, the results presented have established the starting point for further theoretical development to formulate such a function and to build closed-form analytical permeability models for anisotropic porous media based on first principles.

I. INTRODUCTION

Fluid flow in porous media is commonly described by the widely accepted Darcy law, which was originally derived through experiments by Henry Darcy [1] and has been shown to be deducible from the Navier Stokes equations using the homogenization technique [2]. The permeability K, defined by this law, for an isotropic medium is quantified by theoretical models mostly based on the Kozeny-Carman (KC) formula [3, 4],

$$K = \frac{f(\phi)}{kS^2} \tag{1}$$

where k is known as the Kozeny-Carman constant, S is the particle specific area (total area of the grain particles divided by their total volume), and $f(\phi)$ is a porosity function [5]. The value for k is usually taken as proportional to the square of the tortuosity T, introducing in that way the medium's pore structure into Eq. 1. The relationship expressed in Eq. 1 is based on the assumption of a Poiseuille flow through a pipe [6, 7]. Moreover, the porosity function $f(\phi)$ has many proposed forms, including the theoretically derived Kozeny-Carman porosity function $f(\phi) = c_0\phi^3/(1-\phi)^2$, with c_0 being a shape parameter [7], and empirical power law relations [5, 8].

In anisotropic media, the permeability is a tensor accounting for the difference in the resistance of granular particles to flows in different directions. The tensorial law has been tested previously with numerical studies based on pore network models involving even high Reynolds number flows where the tensorial law is extended with the Forchheimer term [9, 10] and it has been proposed that its tensorial nature is given by an anisotropic tortuosity tensor [6]. However, more detailed studies at the pore scale are needed to elucidate this morphological relationship. At this scale, the flow is strongly dependent on not only details of the topology of the pore structure but also the morphology of the obstacles. These microscopic details, largely inaccessible during physical experiments or macro-scale numerical modelling [11], can be resolved by pore scale simulation techniques.

The overall goal of this article is to quantify the microscopic and macroscopic effect of anisotropic medium morphology on pore-water flow in different directions within the porous media. Simulations were carried out systematically to examine the responses of modelled anisotropic porous media to different pressure gradients applied. The study adopted the Lattice Boltzmann Method (LBM) to model flow through granular assemblies artificially constructed using the Voronoi tessellation method. Anisotropy was introduced at the particle level by altering individual particles aspect ratios, generating samples with isotropic to highly anisotropic pore structures. By taking Eq. 1 as a theoretical basis, the simulation results were analysed to examine the relationship of permeability with the three key morphological variables: the particle specific area S, porosity ϕ and tortuosity tensor $\boldsymbol{T}$.

In the following, Section II explains the methodology, describing how the fluid was modelled with the Lattice Boltzmann Method, how the anisotropic granular medium was constructed with the Voronoi tessellation and how the simulations were carried out. Section III shows the results for the anisotropic permeability tensor followed by Section IV where these results are analysed based on the KC model. An extension of the work for a double-degree anisotropy is also included in Section V. Finally Section VI presents conclusions drawn from the study.

*Electronic address: s.galindotorres@uq.edu.au

II. METHODOLOGY

A. Lattice Boltzmann Method

The LBM has been used previously to study flow effects at the pore scale [11, 12]. For the present study the Lattice Boltzmann D3Q19 scheme was used [13]. In this scheme the space is divided into a cubic domain where each cell has a set of probability distribution functions f_i, representing the density of fluid particles going through one of the 19 discrete velocities $\vec{\boldsymbol{e}}_i$. The density ρ and velocity $\vec{\boldsymbol{u}}$ at each cell position $\vec{\boldsymbol{x}}$ can be determined by:

$$\begin{array}{ll}\rho(\vec{\boldsymbol{x}}) = & \sum_{i=0}^{18} f_i(\vec{\boldsymbol{x}}) \\ \vec{\boldsymbol{u}}(\vec{\boldsymbol{x}}) = & \frac{\sum_{i=0}^{18} f_i(\vec{\boldsymbol{x}})\vec{\boldsymbol{e}}_i}{\rho(\vec{\boldsymbol{x}})}\end{array} \tag{2}$$

Each distribution function has an evolution rule derived from the Chapman Enskog expansion of the Boltzmann equation [14],

$$f_i(\vec{\boldsymbol{x}} + \vec{\boldsymbol{e}}_i\delta t, t + \delta t) = f_i(\vec{\boldsymbol{x}}, t) + \Omega_{col}, \tag{3}$$

where $\vec{\boldsymbol{x}}$ is the position of the local cell, δ_t is the time step and Ω_{col} is a collision operator representing the relaxation processes due to the collision of the fluid particles. For this study, the widely accepted Bhatnagar-Gross-Krook (BGK) model for the collision operator [15] was used, which assumes that the collision processes drive the system into an equilibrium state described by an equilibrium function f_i^{eq},

$$\Omega_{col} = \frac{f_i^{eq} - f_i}{\tau} \tag{4}$$

with τ being the characteristic relaxation time. It has been shown that the Navier Stokes (NS) equations for fluid flow [16] are recovered if,

$$f_i^{eq} = \omega_i\rho\left(1 + 3\frac{\vec{\boldsymbol{e}}_i \cdot \vec{\boldsymbol{u}}}{C^2} + \frac{9(\vec{\boldsymbol{e}}_i \cdot \vec{\boldsymbol{u}})^2}{2C^4} - \frac{3u^2}{2C^2}\right) \tag{5}$$

and the kinetic viscosity of the fluid (ν) is given by,

$$\nu = (\tau - 0.5)\frac{\delta_x^2}{3\delta_t} \tag{6}$$

with $C = \delta_x/\delta_t$, a characteristic lattice velocity defined by the grid spacing δ_x. Eq. 6 imposes a constrain on the choice of τ, which must be greater than 0.5 for the viscosity to be physically correct. It is also known that values close to 0.5 produce unstable numerical behaviour [14] due to the non-linearity of the NS equations; hence it is advisable to keep its value close to one.

The fluid is assumed to be reflected by the solid boundaries. Hence, the bounce-back boundary condition [14] was implemented for cells that are tagged as solids. In the bounce-back condition, after the collision step, the distribution functions are swapped symmetrically as,

$$f_{-i} = f_i \tag{7}$$

where the subscript $-i$ refers to the opposite direction to the i-th velocity.

The simulation domain consisted of a cube of 200 × 200 × 200 LBM cells and pressure (density) boundary conditions were applied to the surface of the cube across each of the principal directions as explained in [17]. The relation between the density and pressure p for this D3Q19 model is given by the ideal gas law $p = C^2\rho/3$. The macroscopic velocity $\vec{\boldsymbol{v}}_m$ and density ρ_m were measured as volume averages over the total number of non solid cells (N_c) [11],

$$\begin{array}{ll}\rho_m = & \sum_{\vec{\boldsymbol{x}}} \rho(\vec{\boldsymbol{x}})/N_c \\ \vec{\boldsymbol{v}}_m = & \frac{\sum_{\vec{\boldsymbol{x}}} \rho(\vec{\boldsymbol{x}})\vec{\boldsymbol{u}}(\vec{\boldsymbol{x}})}{\sum_{\vec{\boldsymbol{x}}} \rho(\vec{\boldsymbol{x}})},\end{array} \tag{8}$$

which were then used to obtain the macroscopic flux $\vec{\boldsymbol{F}} = \rho_m\vec{\boldsymbol{v}}_m$. It was assumed that equilibrium is reached when the following condition is met:

$$\frac{|\vec{\boldsymbol{F}}(t) - \vec{\boldsymbol{F}}(t - 500)|}{|\vec{\boldsymbol{F}}(t)|} < 10^{-5} \tag{9}$$

B. Voronoi Construction of Porous Media

The granular medium consisted of solid particles produced by the Voronoi tessellation. As explained in [18–20], for the construction of a granular assembly an initial cubic grid is filled with points at random positions restricted to one point per cell. Then the Wigner-Seitz polyhedron is calculated for each random point. If there are the same number of cells in the x, y and z direction, then the construction is fairly isotropic. By adding more cells along the z direction but keeping the same cubic dimensions for the domain, the cells become rectangular boxes and the obtained Voronoi polyhedra is now deformed. The ratio between the cell numbers along the z and the horizontal directions (α) determines the mean ratio between the vertical and horizontal dimensions of the solid particles. Fig. 1 shows two Voronoi assemblies for $\alpha = 1.0$ (isotropic) and 5.0 (anisotropic) conditions. The Voronoi construction ensures a random division of the space, and hence, by modifying the random seed of the original points, different Voronoi constructions can be obtained. Because the Voronoi space partition produces a perfect division without any voids, each particle is shrunk by a given length $d_s/2$ to produce pore space for the fluid to go through. The shrunk particles are shown in Fig. 2 for a 2D Voronoi construction as an example. As can be seen in the figure, the fluid can flow through the paths opened by the shrinking process. In this study, the shrinkage length d_s was chosen to be the size of 8 LBM cells (i.e. 8 l.u.) in a domain grid of $200 \times 200 \times 200$ LBM cells, which was appropriate for simulating a Stokes flow in the pore space [14]. Simulations with larger numbers of LBM cells for the domain and hence the pore (with $d_s = 10$ and 12 l.u. respectively) were also conducted. Variations of the predicted permeability simulated with

the different models were small, confirming that the simulations results were sufficiently accurate and resolution-independent.

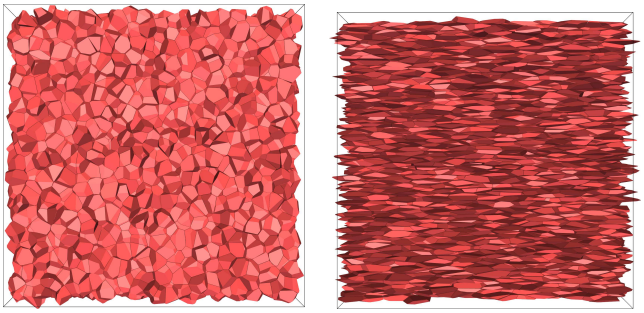

(a)$\alpha = 1.0$ (b)$\alpha = 5.0$

Figure 1: (Color online) Voronoi assemblies (with shrinkage) in 3D for an isotropic ($\alpha = 1.0$) and anisotropic ($\alpha = 5.0$) media.

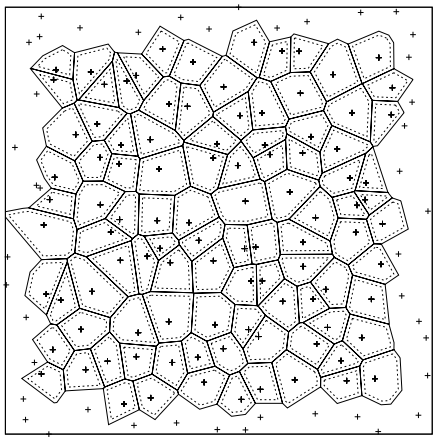

Figure 2: A 2D Voronoi construction with shrinkage shown by the dashed lines. The construction starts with distributing randomly a set of points (crosses) in the domain. A Voronoi polygon is built by the bisection of the lines joining a given point to its neighbours until a convex hull is obtained. Subsequently the polygons are shrunk by a size of $d_s/2$ to obtain a new set of polygons (dashed lines), forming void spaces for fluid flow paths.

C. Simulations

For the flow simulations eight different pressure configurations were used for each aspect ratio (α) value for the porous medium. Furthermore, each of these pressure configurations was combined with 8 random Voronoi samples. The mean value and standard deviation of the results from these eight simulations were calculated and used in the further analysis. The pressure gradient ∇p was defined as the vector (p_x, p_y, p_z) where p_i is the difference between the pressures at the two pressure boundary faces of the cubic domain along the i direction divided by the domain's length ($\Delta p_i/L$). Each of the different pressure configurations has a constant pressure gradient norm ($|\nabla p|$ = constant) but a different angle of a octahedral plane (see Fig. 3). To achieve this, the following relationships were applied:

$$\begin{aligned} p_x &= \frac{p_{iso}}{\sqrt{3}} + \frac{2p_{dev}\sin(\theta - 5\pi/6)}{\sqrt{6}} \\ p_y &= \frac{p_{iso}}{\sqrt{3}} + \frac{2p_{dev}\sin(\theta - \pi/6)}{\sqrt{6}} \\ p_z &= \frac{p_{iso}}{\sqrt{3}} + \frac{2p_{dev}\sin(\theta + \pi/2)}{\sqrt{6}} \end{aligned} \tag{10}$$

The norm $|\nabla p| = \sqrt{p_{iso}^2 + p_{dev}^2}$ is a function of the gradient's isotropic p_{iso} and deviatoric p_{dev} components, independent of the θ angle of the octahedral plane. The parameters used in the simulations are given in Table I.

Table I: Set of parameters used in the simulations with values given in lattice units of length (l.u.), time (t.u.) and density (d.u.). The constant C (see Eq. 5) was set as one. The values for p_{iso} and p_{dev} ensured that the simulations were conducted within the incompressible limit and with small Reynolds numbers.

Parameter	Value
δ_x	1.0 l.u.
δ_t	1.0 t.u.
τ	1.0
d_s (spacing between obstacles)	8 l.u.
p_{iso}	0.02 d.u.$\times C^2/3$
p_{dev}	0.01 d.u.$\times C^2/3$
ρ_0 (initial density)	1.0 d.u.

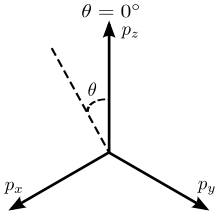

Figure 3: Octahedral plane for the pressure gradient space. For the simulations, 8 different θ angles were considered for each aspect ratio α.

To determine the permeability tensor $\boldsymbol{K}$, only three θ angles were needed. Thus, the results with the other 5 angles were used to validate the derived tensor. Darcys law was used for computing $\boldsymbol{K}$,

$$\boldsymbol{K}\nabla p = \mu \vec{\boldsymbol{v}}_m, \tag{11}$$

where the dynamic viscosity μ is related to the kinematic viscosity ν by the fluid's density $\mu = \rho_m \nu$. To illustrate the method, the numerical results for $\alpha = 2.0$ are shown in Tables II, III and IV. Table II shows the components of vector $\mu\vec{\boldsymbol{v}}_m$ obtained by averaging the simulated flow at all cells across the domain for different θ values. As explained above, only three flow vectors for three different

angles θ were required to determine $\boldsymbol{K}$; in the presented cases $\theta = 105°$, $150°$ and $195°$ were used. Table III shows the obtained $\boldsymbol{K}$ tensor, and table IV shows the velocity vectors calculated from the product $\boldsymbol{K}\nabla p$. Fig. 4 shows for all aspect ratios the difference between measured and predicted velocity. The relative difference in velocity was small ($< 3.5\%$) for conducted simulations, indicating that Darcy's law applies in the simulated value range of parameters. Note that the norm of a tensor $|\boldsymbol{A}|$ used is the standard Euclidean norm, i.e., $\sqrt{\sum_{ij} A_{ij}^2}$. Also shown in Fig. 4 is the variation of the density ρ_m. Since this variation is also small, it can be concluded that the simulations were conducted within the incompressible limit.

Table II: Components of the $\mu\vec{\boldsymbol{v}}_m$ vector (in units of 10^{-4} d.u. $\times$ l.u.^{3} $\times$ t.u.$^{-2}$) obtained from simulations for each of the 8 θ values and $\alpha = 2.0$.

	15°	60°	105°	150°	195°	240°	285°	330°
$\mu \cdot v_x$	0.1850	0.2775	0.2943	0.2257	0.1118	0.0024	0.0711	0.0193
$\mu \cdot v_y$	0.2536	0.1460	0.0394	-0.0037	0.0419	0.2563	0.2993	0.1497
$\mu \cdot v_z$	0.0028	0.0109	0.0609	0.1235	0.1621	0.1038	0.0412	0.1539

Table III: Calculated permeability matrix $\boldsymbol{K}$ based on simulation results for $\alpha = 2.0$. The non-diagonal terms are not exactly zero but are much smaller than the diagonal components, indicating that the simulation system is close to the principal coordinate system as expected. Furthermore, the first two diagonal terms are very similar but the third is notably smaller, consistent with the mediums anisotropic configuration. The eigenvalues of this matrix are 0.4567, 0.4436 and 0.2474 (in units of l.u.^{2}), which is very close to the diagonal values.

$$\boldsymbol{K} = \begin{pmatrix} 0.4492 & -0.0062 & 0.0021 \\ -0.0068 & 0.4510 & -0.0006 \\ -0.0004 & 0.0004 & 0.2474 \end{pmatrix}$$

Table IV: Components of the $\mu\vec{\boldsymbol{v}}_m$ vector (in units of 10^{-4} d.u. $\times$ l.u.^{3} $\times$ t.u.$^{-2}$) calculated from the product $\boldsymbol{K}\nabla p$ for $\alpha = 2.0$. The calculated flow vectors are identical to the simulated ones for $\theta = 105°$, $150°$ and $195°$ as expected by construction, and they only slightly differ in the other cases. This confirms the validity of the Darcy law in the tensorial form of Eq. 11.

	15°	60°	105°	150°	195°	240°	285°	330°
$\mu \cdot v_x$	0.1850	0.2775	0.2943	0.2257	0.1118	0.0025	0.0711	0.0193
$\mu \cdot v_y$	0.2538	0.1461	0.0394	-0.0037	0.0419	0.2563	0.2994	0.1496
$\mu \cdot v_z$	0.0028	0.0109	0.0609	0.1235	0.1621	0.1040	0.0414	0.1540

III. RESULTS

As explained in the previous section, a permeability matrix can be determined for each sample with given

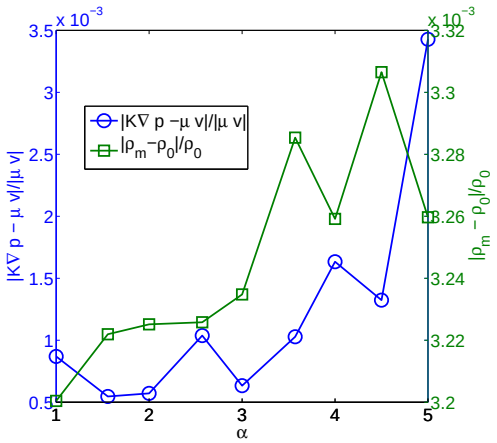

Figure 4: (Color online) Relative differences between the fluid velocity simulated and calculated by Darcys law (circles), and between the measured density ρ_m and the initial density ρ_0 (squares) for cases of different aspect ratios α.

aspect ratio α. The material parameters are the eigenvalues (K_i) of this matrix. Fig. 5 shows these eigenvalues for the values of α used in the simulations. As expected, the first two eigenvalues, corresponding with the x and y axis, are very close since anisotropy is introduced in the discussed simulations only along the z axis. The third eigenvalue K_3 is associated with the permeability along z. With an increasing aspect ratio α, the solid particles become more stretched horizontally and their surface area perpendicular to the z direction increases, resulting in higher resistance to the flow in this direction. To overcome the obstacles, the flow takes a larger path around them. This is the reason why the K_3 eigenvalue decreases with the aspect ratio α. As shown in the next section, the tortuosity behaves differently along the principal directions, which in turn produces the anisotropy of the permeability tensor.

The evolution of K_i shown in Fig. 5 seems to be not monotonous: at $\alpha = 3.5$ a sudden variation of the trends for all three eigenvalues can be recognised. This effect is a consequence of the Voronoi division of space. The total number of solid particles placed into the domain is given by $N_o = N_h^3 \alpha$ where N_h is the number of particles along the horizontal direction. In the simulations, N_o was set to be as close to 1000 obstacles as possible. However, N_o changes for different α. For instance, for $\alpha = 3.5$ $N_o = 1225$ while for $\alpha = 4.0$ $N_o = 864$. This sudden change in the number of particles leads to variations in the porosity since the domain's volume remains constant. Fig. 6 shows the variation of the porosity ϕ with α. A decrease in porosity is evident from $\alpha = 3.5$ to $\alpha = 4.0$, illustrating the effect of the Voronoi construction.

Before proceeding with the analysis, it is useful to check how close the samples are to a principal system as defined by the coordinates/axes (x, y and z). Such a principal system possesses a permeability tensor of

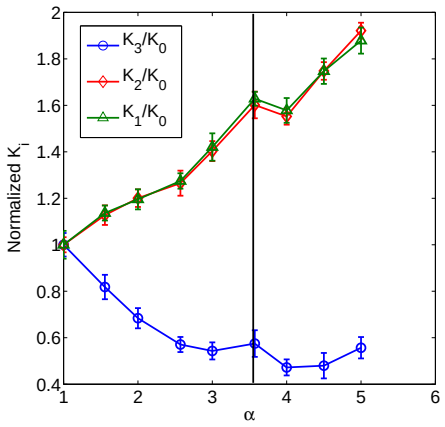

Figure 5: (Color online) Eigenvalues K_i of the permeability matrix/tensor $\boldsymbol{K}$ found for each aspect ratio α normalized by the isotropic permeability K_0. The error bars show the standard deviations among the simulated random Voronoi samples.

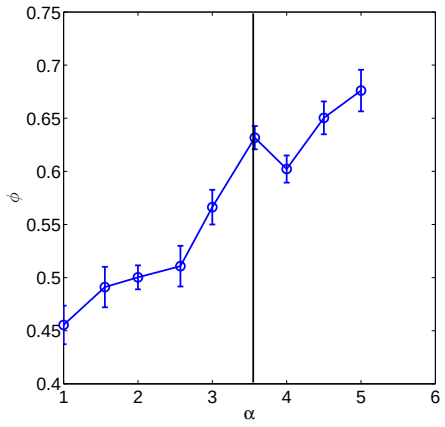

Figure 6: (Color online) Porosity ϕ versus aspect ratio α.

only diagonal elements given by the eigenvalues, i.e. $\boldsymbol{K} = \boldsymbol{K}_{eig} = \text{diag}(K_1, K_2, K_3)$. Fig. 7 shows that the relative difference between $\boldsymbol{K}$ and $\boldsymbol{K}_{eig}$ was less than 3.5%. Therefore it is justified to say that the solid particles placement and configuration modelled here ensured a sample principal system consistent with the defined coordinates.

IV. ANALYSIS

The analysis of the simulation results is carried out based on Eq. 1. The three geometric variables that affect the permeability of the system are the specific area S, the porosity ϕ and the tortuosity T. Considering the dimensions of the variables, it can be recognised that the eigenvalues of the permeability tensor, with the dimension $[L^2]$, must be proportional to S^{-2} since S is the only variable with a dimension, $[L^-1]$. Therefore, an equation similar to the KC model is inferred for the eigenvalue K_i:

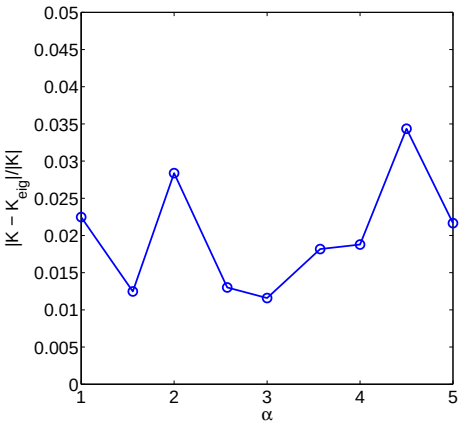

Figure 7: (Color online) Normalized difference between the computed permeability tensor $\boldsymbol{K}$ and the corresponding eigenvalue tensor $\boldsymbol{K}_{eig}$.

$$K_i = f(\phi) S^{-2} g(T_i) \tag{12}$$

where it is assumed that the anisotropy of $\boldsymbol{K}$ depends solely on the anisotropic nature of the tortuosity tensor $\boldsymbol{T}$, a hypothesis that has been proposed previously [6]. The ratio between the smallest eigenvalue K_3 and the mean horizontal eigenvalue $K_t = (K_1 + K_2)/2$ should then be a function of the tortuosity, independent of the specific area or porosity, i.e.,

$$\frac{K_3}{K_t} \sim \frac{g(T_z)}{g(T_t)}. \tag{13}$$

In Eq. 13 T_z is the tortuosity in z direction, and T_t is the mean horizontal tortuosity.

Fig. 8 shows the K_3/K_t ratio. The sudden changes due to the porosity evolution shown in Fig. 5 almost disappear and now a monotonic function is obtained, which supports the underlying hypothesis behind Eq. 13

It is necessary at this point to measure the tortuosity in the different directions. From the results shown in Fig. 7, it can be concluded that the simulation coordinate system is the same as the sample's principal system. For such a principal system, the tortuosity tensor $\boldsymbol{T}$ must be diagonal as well. Thus by applying the pressure gradient along each principal direction to generate the flow and measuring the streamlines' length given by the flow field, the tortuosity tensor components can be readily derived. The streamlines can be computed by evaluating the line integral of the velocity field with a fourth order Runge-Kutta scheme. To obtain the velocity at any point in the domain, a trilinear interpolation is used based on the velocities at each cell. Fig. 9 illustrates the method to calculate the streamline length and tortuosity.

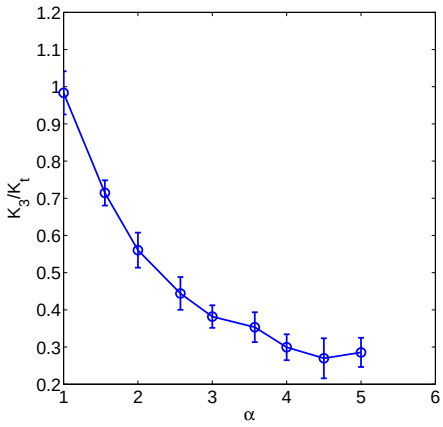

Figure 8: (Color online) Permeability ratio, K_3/K_t, versus the aspect ratio α.

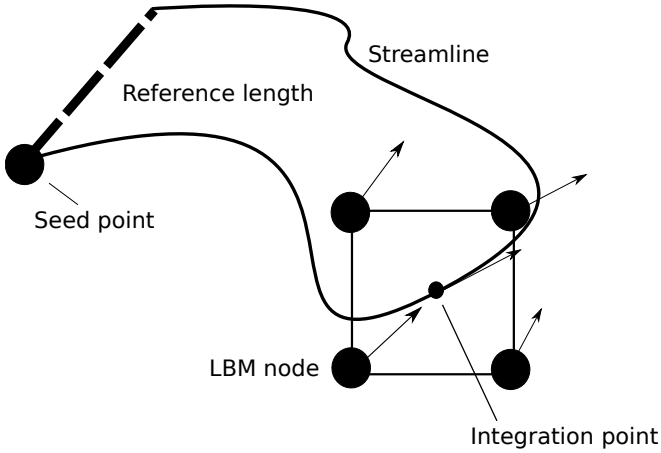

Figure 9: A streamline is constructed by starting with a seed point at the domain boundary. Then the pathline of the seed, representing a streamline, is then determined by solving the differential equation $\frac{\partial \vec{x}}{\partial t} = \vec{v}$ numerically. To obtain the velocity at the integration point, a trilinear interpolation is used with the velocities at the closest 8 LBM nodes. Once the streamline is obtained, the length is given by the line integral, and the tortuosity by dividing the streamline length over the straight distance between the two streamline ends (dashed line).

Other definitions for the tortuosity used in the literature include the average of the streamline length weighted by the time it takes for a particle in the streamline to move cross the domain [12]. The definition of the tortuosity may have important consequences on the permeability tensor values, but the general form described in Eq. 12 should remain unchanged.

Fig. 10 shows the tortuosity along the z axis (T_z) and the average horizontal tortuosity (T_t). It is clear that the tortuosity component T_z increases with the aspect ratio α. For $\alpha = 5.0$, the average streamline driven by a pressure gradient across the z direction is 1.8 times longer than the average streamline associated with flow driven by a gradient in the x direction. This agrees with the result shown in Fig. 11 where the effect of a rectangular solid particle on local flows and streamlines is evident. An anisotropic particle opposes the flow in the z direction, lengthening the associated streamlines around it. In an assembly of particles forming an anisotropic media, the tortuosity is not only a function of the particle shape, pore space morphology and flow direction also influence the tortuosity. On the other hand, as can be seen in Fig. 10 the horizontal tortuosity slightly decrease as the particles become flatter and hence provide less resistance to the fluid along the x or y direction.

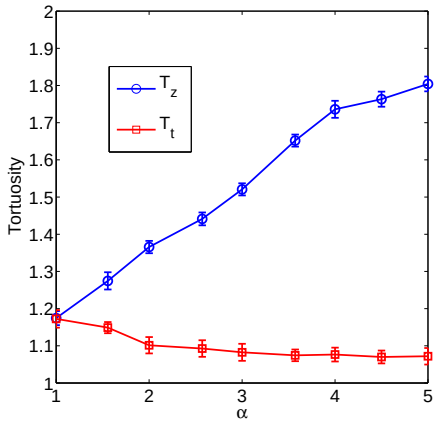

Figure 10: (Color online) Vertical T_z and horizontal T_t tortuosities versus the aspect ratio α.

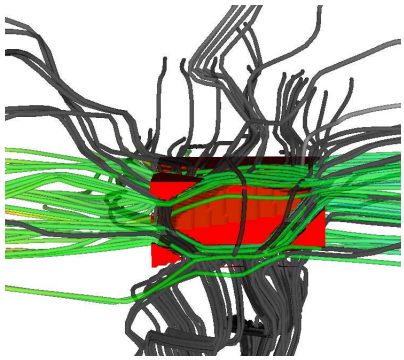

Figure 11: (Color online) Streamlines across a single solid particle for a gradient across the z direction (dark) and across the x direction (light). The aspect ratio of the particle is $\alpha = 4.0$.

To determine the g function of Eq. 13, the relationship between the permeability ratio and the tortuosity ratio is examined in Fig. 12. A power function with exponent equal to -2.0 was found to describe well the relationship, which is consistent with the KC model of Eq. 1. This exponent value in the KC model is based on the assumption of Poiseuille pipe flow traversing the porous

medium, which is an assumption valid for the anisotropic medium as well, at least within the low Reynolds number constrain applied in the present study.

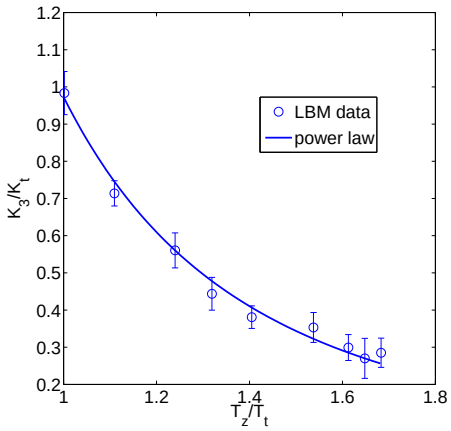

Figure 12: (Color online) Permeability ratio K_3/K_t versus tortuosity ratio T_z/T_t. The fitting model is given by a power function with exponent equal to -2.0 ± 0.1.

To determine the porosity function $f(\phi)$, a normalization procedure, described in the following, is applied. Based on Eq. 12, a set of dimensionless parameters Λ_i can be calculated based on the simulation results, which is related to the porosity function:

$$\Lambda_i = K_i S^2 T_i^{2.0} = f(\phi). \tag{14}$$

The particle specific area S can be calculated based on the simulation setup since the area of each particle is known. S increases with the aspect ratio α as shown in Fig. 13. As $\alpha \to \infty$, the volume goes to zero and $S \to \infty$ assuming that the surface area remains constant. However, the number of particles is not constant, nor is the particle surface area. Thus the same sudden decrease of S can be observed at $\alpha = 3.5$ as on the conductivity and porosity curves (Figs. 5 and 6). Note that the trend shown in Fig. 13 is characteristic for media generated by the Voronoi construction method used here; and other particle generation methods may lead to different S vs. α relationships.

With S, K_i and T_i computed, Eq. 14 is used to calculate Λ_i, which is shown as a function of the porosity in Fig. 14. The results show that the difference due to the anisotropic medium disappears and the parameters (Λ_i) for the three directions behave in the same way. The KC porosity function, $f(\phi) = c_0\phi^3/(1-\phi)^2$ with the shape factor c_0 as a free fitting parameter, appears to fit well the calculated results. In this connection, the shape factor c_0 depends on the porous media morphology. Kozeny proposed values between 1/2 and 1/6, which have been shown to agree with experimental results [3, 6] . In the present work, a value of $c_0 = 0.22 \pm 0.02$ was found through curve-fitting. The simulated medium built with the Voronoi construction method appears to have a similar behaviour to that of packed spheres with similar porosity and specific area.

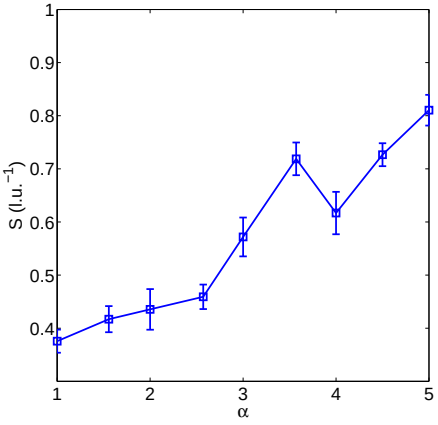

Figure 13: (Color online) Specific area S versus the aspect ratio α.

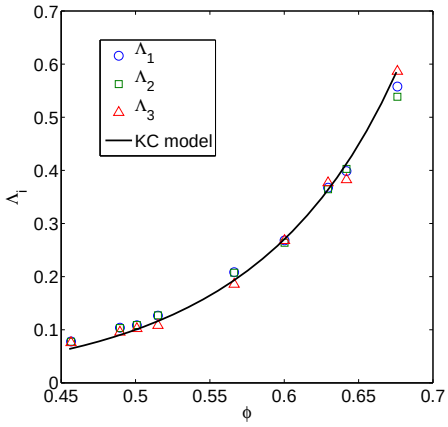

Figure 14: (Color online) Calculated Λ values versus porosity. The KC porosity function $f_{KC}(\phi) = 0.22\phi^3/(1-\phi)^2$ is shown as the fitted function.

V. DOUBLE ANISOTROPY

Based on the above simulations that considered a single degree of anisotropy only, a permeability model for anisotropic porous media was established, involving a relation between the tortuosity tensor $\boldsymbol{T}$ and the permeability $\boldsymbol{K}$:

$$\boldsymbol{K} = c_0 \frac{\phi^3}{(1-\phi)^2 S^2} \boldsymbol{T}^{-2}. \tag{15}$$

In this section, we discuss simulations incorporating double anisotropy induced along the y direction as well as the z direction. The aim of these simulations was to

further test the validity of Eq. 15. The average particle dimension along the y direction was set to be twice as large as the average x dimension introducing an aspect ratio $\beta = 2$. In the simulations, the anisotropic factor β along the y direction was kept constant and the anisotropy (α) along the z direction varied from 1.0 to 5.0 as in the simulations presented before. To validate Eq. 15, both the porosity ϕ and specific area S were determined for each simulation. The results are shown in Fig. 15. Again the low number of particles produced a sudden changes at various values of α as observed before for $\alpha = 3.5$ in the single anisotropy case. For the double anisotropy model, sudden increases of S and ϕ were evident at $\alpha = 2.0$ and 4.0.

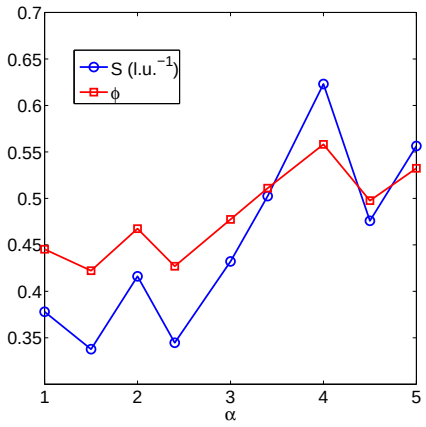

Figure 15: (Color online) Specific area S and porosity ϕ for lateral anisotropy factor $\beta = 2.0$ and varying vertical anisotropy factor α.

The third variable to be determined in order to check Eq. 15 is the tortuosity. The same strategy used above was applied to this case: gradients were applied along the principal directions with the tortuosity subsequently measured along these directions. The results are shown in Fig. 16. In contrast to the result shown before, the three components are different here, although for $\alpha = 1.0$ T_x and T_z are equal and T_y is higher due to the anisotropy along the y direction ($\beta = 2$). At this point $T_y = 1.4$, close to the value of T_z for the single anisotropy case with $\alpha = 2$ shown in Fig. 10, meaning that the two cases are identical as physically expected. Also, the value for T_z and T_x is close to the value for T_x and T_y in Fig. 10 with $\alpha = 2$ for the same reason. Furthermore, the curves of T_z and T_y intersects at $\alpha = \beta = 2.0$ as expected. Although the second anisotropy factor β was kept constant, the tortuosity along this direction decreased slightly. As the particles were compressed along the z direction, it was easier for the fluid to flow along the x and y directions with streamlines of less tortuosity. The maximum value for T_z is 1.64, considerably smaller than the maximum value of 1.8 found in the single anisotropy simulations. Due to the reduction of the particles' y dimension, the maximum tortuosity in the z direction is reduced.

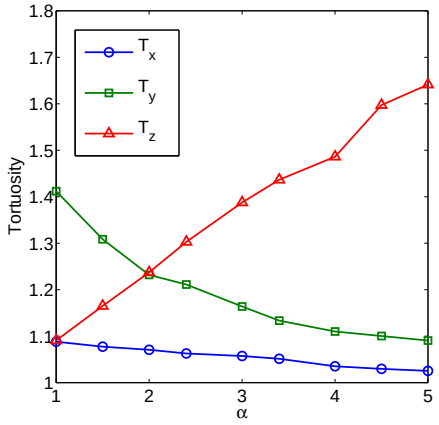

Figure 16: (Color online) Tortuosity components for lateral anisotropy factor $\beta = 2.0$ and varying vertical anisotropy factor α.

Finally, the results of Figs. 15 and 16 are combined with Eq. 15 to obtain the components of the permeability tensor for the case of double anisotropy. This permeability tensor is compared with the values predicted by the simulations in Fig. 17. Overall the KC model seems to agree fairly well with the simulated permeability components. Both simulated and calculated conductivities have peaks at $\alpha = 2.0$ and 4.0 due to the evolution of S and ϕ with increasing α (Fig. 15). The difference between the three components can be related to the tortuosities. Both K_x and K_y increased due to the decrease of their corresponding tortuosities and the overall increase of S and ϕ. In contrast, S and ϕ cannot overcome the effect of the increase of T_z on K_z, resulting in a decreasing trend for the permeability in the z direction.

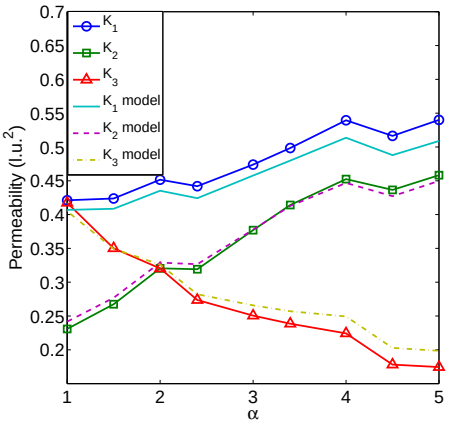

Figure 17: (Color online) Permeability components for lateral anisotropy factor $\beta = 2.0$ and varying vertical anisotropy factor α: comparison between the values simulated by the LBM model and calculated by Eq. 15.

VI. CONCLUSIONS

In the present work, LBM simulations of flow through anisotropic porous media have been carried out. The media were constructed with the Voronoi tessellation method in 3D, which produces a random and yet controllable internal morphology of solid particles and associated pore space. The assembly's anisotropy was introduced at the particle/pore scale by imposing a mean particle aspect ratio α. The results were analysed based on the well-known Kozeny Carman (KC) model, originally developed for isotropic media (Eq. 1). The results demonstrate that the KC model also describes the permeability tensor $\boldsymbol{K}$ well for the simulated anisotropic media, with the anisotropic nature represented by the tortuosity tensor $\boldsymbol{T}$ (Eq. 15).

This finding suggests that the assumptions made in the formulation of the KC model hold as well for flow through the anisotropic media simulated by the Voronoi construction method. In particular, the flow can be assumed to behave like the Poiseuille flow through pipes, which can represent the streamlines shown in Fig. 11. These assumptions justify the dependence of K on the tortuosity and the inverse of the specific area as well as the KC porosity function $f(\phi) = c_0\phi^3/(1-\phi)^2$. Although the specific area does not have a simple analytical expression like that for the sphere case, it can be calculated nonetheless from the area and volume of each solid particle. The tortuosity tensor was measured in its principal system; however, the above law is generally valid for any coordinate system.

A more general sample with anisotropy in two directions was used to check the validity of Eq. 15. Again the three variables S, ϕ and $\boldsymbol{T}$ were determined independently. Eq. 15 seems to agree with the measured/simulated permeability components in this more general case. Although both anisotropy factors α and β were kept larger than one, this represents a general case. Systems with anisotropy factors smaller than one can be obtained by rotating the studied samples because of the physical laws symmetry.

Previous studies have proposed analytical relationships between the tortuosity and the porosity for isotropic media [12]. However, as the numerical results of this study show, tortuosity is a complex function of both porosity and solid particle morphology. Future studies should be conducted to explore further the definition of the tortuosity tensor based on the conductivity. In the present work, the traditional definition for tortuosity was taken, but there are more advanced definitions in the literature and they could affect the dependence of K on T. Future research can also apply the methodology proposed here to study anisotropic flow in unsaturated conditions using the multiphase-multicomponent LBM scheme. Under unsaturated flow conditions, the full connectivity assumed in saturated conditions no longer applies and a percolation term may need to be included in the conductivity tensor.

Acknowledgments

This work was funded by the UQ Early Career Research Grants Scheme (RM2011002323). The simulation code was programmed using the LBM module from the MechSys open source library (`http://mechsys.nongnu.org/index.shtml`) developed by the first author. The Voronoi tessellation was obtained from the *Voro++* open source library (`http://math.lbl.gov/voro++/`) developed by Chris Rycroft.

[1] H. Darcy. Les fontaines de la ville de dijon. *Victor Dalmont, Paris*, 1856.

[2] S. Whitaker. Flow in porous media i: A theoretical derivation of darcy's law. *Transport in porous media*, 1(1):3–25, 1986.

[3] J. Kozeny. Über kapillare Leitung des Wassers im Boden. *Akad. Wiss. Wien*, 136:271–306, 1927.

[4] Mohammad Mehdi Ahmadi, Soheil Mohammadi, and Ali Nemati Hayati. Analytical derivation of tortuosity and permeability of monosized spheres: A volume averaging approach. *Phys. Rev. E*, 83:026312, Feb 2011.

[5] F.A.L. Dullien. *Porous media: fluid transport and pore structure*, volume 26. Academic press, 1992.

[6] J. Bear. *Dynamics of fluids in porous media*. Dover publications, 1988.

[7] PC Carman. Permeability of saturated sands, soils and clays. *J. Agric. Sci*, 29:262–273, 1939.

[8] H. C. H. Rumpf and A. R. Gupte. Einflsse der porositt und korngrenverteilung im widerstandsgesetz der porenstrmung. *Chemie Ingenieur Technik*, 43(6):367–375, 1971.

[9] X. Wang, F. Thauvin, and KK Mohanty. Non-darcy flow through anisotropic porous media. *Chemical Engineering Science-Paper Edition*, 54(12):1859–1870, 1999.

[10] M. Balhoff and M. Wheeler. A predictive pore-scale model for non-darcy flow in anisotropic media. In *SPE Annual Technical Conference and Exhibition*, 2007.

[11] JE McClure, WG Gray, and CT Miller. Beyond anisotropy: examining non-darcy flow in asymmetric porous media. *Transport in porous media*, 84(2):535–548, 2010.

[12] Artur Duda, Zbigniew Koza, and Maciej Matyka. Hydraulic tortuosity in arbitrary porous media flow. *Phys. Rev. E*, 84:036319, Sep 2011.

[13] M. Hecht and J. Harting. Implementation of on-site velocity boundary conditions for d3q19 lattice boltzmann simulations. *Journal of Statistical Mechanics: Theory and Experiment*, 2010:P01018, 2010.

[14] M.C. Sukop and D.T. Thorne. *Lattice Boltzmann modeling: An introduction for geoscientists and engineers*. Springer Verlag, 2006.

[15] Y.H. Qian, D. d'Humieres, and P. Lallemand. Lattice bgk models for navier-stokes equation. *EPL (Europhysics Letters)*, 17:479, 1992.

[16] X. He and L.S. Luo. Lattice boltzmann model for the incompressible navier–stokes equation. *Journal of Statistical Physics*, 88(3):927–944, 1997.

[17] P.M. Gresho and R.L. Sani. On pressure boundary conditions for the incompressible navier-stokes equations. *International Journal for Numerical Methods in Fluids*, 7(10):1111–1145, 1987.

[18] SA Galindo-Torres and DM Pedroso. Molecular dynamics simulations of complex-shaped particles using Voronoi-based spheropolyhedra. *Physical review. E, Statistical, nonlinear, and soft matter physics*, 81(6 Pt 1):061303, 2010.

[19] S.A. Galindo-Torres, D.M. Pedroso, D.J. Williams, and L. Li. Breaking processes in three-dimensional bonded granular materials with general shapes. *Computer Physics Communications*, 183(2):266 – 277, 2012.

[20] C.H. Rycroft. Voro++: A three-dimensional voronoi cell library in c++. *Chaos*, 19:041111, 2009.